PHYSICAL REVIEW B VOLUME 60, NUMBER 8 15 AUGUST 1999-II

Observation of an extraordinary antiferromagnetic transition on the NiO(100) surface by metastable helium atom diffraction

M. Marynowski, W. Franzen, and M. El-Batanouny
Department of Physics, Boston University, Boston, Massachusetts 02215

V. Staemmler
Lehrstuhl für Theoretische Chemie, Ruhr-Universität, Bochum, Germany

(Received 24 August 1998; revised manuscript received 16 March 1999)

We report on the temperature dependence of magnetic diffraction peaks obtained by scattering of coherent metastable 2 ^3S helium atomic beams from the (100) surfaces of antiferromagnetic NiO crystals. The data obtained are related to the surface sublattice magnetization using a formalism developed within the framework of the eikonal approximation. The results reveal a surface antiferromagnetic transition that belongs to the universality class of the anisotropic extraordinary surface transition of the three-dimensional Heisenberg model (3D HM) with surface anisotropy ($d=3$, $n=3$, $m_e=1$): A 2D surface spin-ordering transition takes place at 529 K, followed by a crossover to a multicritical regime at the bulk Neél temperature $T_N^b=523.6\,\mathrm{K}$. We obtain the crossover function by plotting the sublattice magnetization m_1, against the crossover scaling variable $|(J_s/J_s^c)-1|/[(T/T_c^b)-1]^\phi$, where J_s is an effective surface exchange coupling, J_s^c is its critical value, T_c^b is the bulk critical temperature, and using the crossover exponent $\phi=0.57$, derived by Diehl and Eisenriegler for the 3D anisotropic HM (AHM). This function is very similar to that reported by Binder and Landau for the 3D Ising model with $\phi=0.56$, and we may ascertain that the critical behavior of the 3D extraordinary transition for both models is quite similar. The critical behavior of the NiO(001) surface reported here is attributed to the presence of single-site spin anisotropy in an otherwise Heisenberg-like surface layer, absent in the bulk because of its higher symmetry. We obtain an estimate of the anisotropy energy of $D=-2.5\,\mathrm{meV}$, by electronic-structure cluster calculations employing Hartree-Fock states with configuration interactions. The fact that the presence of surface single-site anisotropy leads to enhancement of the surface Neél temperature is supported by recent mean-field theoretical studies based on the Schwinger-boson formalism, which indicate that for $D/J>0.1$ the surface Neél temperature is consistently higher than that of the bulk even when the surface superexchange energy is suppressed to 75% of the bulk value. [S0163-1829(99)04532-4]

I. INTRODUCTION

The bulk magnetic properties of the family of antiferromagnetic (AF) $3d$ monoxide crystals, MnO, FeO, CoO, and NiO, with the rock-salt structure have been thoroughly studied over the past four decades.[1–16] These studies, mainly involving thermal neutron scattering, included long-range spin ordering, spin dynamics, and spin-wave dispersion, and the temperature dependence of the sublattice magnetization. Magnetic neutron-diffraction experiments showed that the antiferromagnetic spin ordering consists of ferromagnetic sheets of the magnetic metal atoms parallel to the (111) planes, which are then stacked antiferromagnetically.[1–3,9] Experimental and theoretical studies of the exchange coupling in these oxides lead to our current understanding that nearest-neighbor interactions are ferromagnetic, of the overlap type, while next-nearest-neighbor couplings are antiferromagnetic, of the superexchange type;[10,11] the latter is estimated to be about ten times the strength of the former.[12]

Paramagnetic (P) NiO has the NaCl structure ($Fm3m$, O_h^5), whereas below the Néel temperature, $T_N^b=523\,\mathrm{K}$, the crystal becomes slightly distorted from the cubic structure to a rhombohedral one.[13] This deformation is presumably due to the magnetostriction which accompanies the magnetic order: the amount of the distortion is found to increase with decreasing temperature, and consists of a contraction of the original cubic unit cell along any one of the four ⟨111⟩ axes.

The direction of the sublattice magnetization of the ferromagnetic (111) sheets in NiO lies in the (111) planes. The spins were first assumed by Roth to line up with the ⟨110⟩ direction;[3,4] however, subsequent studies by Yamada showed that the spins line up along the $\langle 11\overline{2}\rangle$ direction.[6] Because of the octahedral site symmetry of the Ni ions, the only contribution to the site anisotropy comes from dipolar interactions among the spins. Early theoretical studies of the AF→P transition based on analysis of the temperature dependence of the ⟨111⟩ magnetic neutron-diffraction peak intensity, measured by Roth, led to the classification of the phase transition as first order.[4] However, more recent neutron-diffraction measurements of the ⟨111⟩, ⟨222⟩, ⟨333⟩, and ⟨444⟩ Bragg peaks using a time-of-flight spectrometer showed that the transition is second order, with a sublattice magnetization exponent $\beta=0.33$.[14] Although the authors prefer to classify this critical behavior as Ising-like, it seems that within the ambiguity of experimental errors, the value $\beta=0.345$ for the Heisenberg system is not out of the question. Moreover, inelastic neutron-scattering measurements of the spin-wave dispersion curves for NiO were reported by Hutchings and Samuelsen.[12] They find that the energy dispersion has a steep initial slope of ∼250 meV Å and a maxi-

©1999 The American Physical Society

mum energy of ~117 meV. They also observe zone-center modes of 4.5 meV associated with out-of-the-(111)-plane anisotropy energy and a 1.5 meV mode associated with in-the-(111)-plane anisotropy energy. Empirical fits to the measured dispersion curves produced the following estimates: second-neighbor superexchange $J_2^b \sim 19.0\,\mathrm{meV}$, first-neighbor ferromagnetic exchange $J_1^b \sim -1.37\,\mathrm{meV}$, out-of-plane site-anisotropy energy $D_1^b \sim 0.1\,\mathrm{meV}$, in-plane site-anisotropy energy $D_2^b \sim 0.006\,\mathrm{meV}$, and an effective spin $\langle S \rangle_z \sim 0.9242$. Moreover, these magnetic parameters were used to determine the Neél temperature: molecular-field-based calculations gave $T_N^b \sim 886\,\mathrm{K}$, while those based on random-phase-approximation Green's-function relations gave $T_N^b \sim 601\,\mathrm{K}$;[15,16] both of these values are consistently higher than the measured value of about 523 K.

Theoretical studies of surface critical behavior of magnetic systems, such as is manifested in the $3d$ oxides, have had a late start.[17–35] This can be attributed, to a large degree, to the lack of experimental measurements. Instead, attention has been devoted to bulk magnetic behavior, and surface effects on bulk critical behavior have been ignored. The argument has been advanced that surface effects will be appreciable only within a bulk correlation length, which for all practical reasons is always much smaller than the physical size of the systems studied since experimentally attainable correlation lengths are of the order of a few thousand angstroms. The factors that influence surface critical behavior can be split into two main categories: The first category consists of ''geometric'' effects involving the breaking of translational symmetry, the reduction of rotational symmetries, and missing neighbors. The second category consists of ''dynamical'' effects manifested by the fact that magnetic interactions at the surface may be quite different from those in the bulk. This raises the possibility that the surface may order before the bulk if the effective surface interactions are stronger than those in the bulk. The thermodynamic average of a local observable at the surface will, in general, be different from its value deep in the bulk; e.g., the local magnetization m_1 at the surface will differ from the bulk magnetization m_b. Correlation functions involving spins at the surface are also expected to be strongly modified. These changes make it necessary to introduce new exponents to describe the critical behavior at the surface, e.g., the exponent β_1 for the surface magnetization. As a consequence of such changes, it has been argued that surface magnetic properties may exhibit a rich phase diagram.

The introduction of probes which are sensitive to local surface observables (as, for example, the mean magnetization in the surface region), such as low-energy electron diffraction (LEED) and spin-polarized LEED (SPLEED), spin-polarized secondary-electron spectroscopy (SPSES), and spin-polarized photoemission spectroscopy (SPPES), and more recently metastable helium atom scattering (MHAS), opened up the possibility of investigating surface magnetic critical behavior experimentally. This, in turn, has spurred theoretical studies of such effects. Until recently, our understanding of these effects was largely based on mean-field theory (MFT) and on the phenomenological theory of scaling (PTS), despite their known shortcomings in predicting the values of the critical exponents.[17–25] Although important information has also come from exact solutions,[24] series analysis,[20,21] Monte Carlo calculations,[27–29] and more recently field-theoretic methods,[30–35] the prime role of these latter techniques was to confirm or refine the physical ideas that had been put forward by MFT and PTS.

MFT predicts three possible regimes for the surface critical behavior. When the effective surface exchange interaction (J_s) is weaker than a critical value (J_s^c), the surface is forced to order at the bulk transition temperature (T_c^b), and the ensuing transition is labeled *ordinary*.[19] However, when $J_s = J_s^c$, the surface orders at T_c^b, independent of the bulk, and we have a multicritical behavior, and the transition is labeled *special*.[23] When $J_s > J_s^c$, we have the onset of a purely two-dimensional transition at a temperature $T_c^s > T_c^b$, followed by a crossover behavior at T_c^b. The latter has been coined an *extraordinary* transition.[19] But MFT is known to be incorrect for bulk properties near T_c^b if the space dimension is below its upper critical value, $d^* = 4$, for short-range interactions. As a matter of fact, MFT wrongly predicts that bulk critical exponents are independent of the dimensionality of the order parameter. A similar breakdown of mean-field theory should occur for local critical properties. For example, although MFT provides a correct qualitative description of the surface critical behavior of a three-dimensional (3D) semi-infinite Ising model, it gives the wrong prediction for the surface critical behavior of the 2D Ising system. Moreover, recent field-theoretic analyses have shown that the surface exponents cannot in general be expressed completely in terms of bulk exponents,[35] contrary to arguments and predictions based on scaling theory.[23,26]

Early studies of the surface spin ordering on the NiO(100) surface were carried out by Palmberg *et al.* in 1968–1971 using LEED.[36–38] These studies reported a (2×1) surface magnetic structure, consistent with a bulk termination. They also reported a surface magnetization exponent $\beta_1 = 1$, the mean-field value; however, the Debye-Waller (DW) factor in the temperature dependence of the (1/2,0) magnetic diffraction peak intensity was not taken into account. Subsequently, Namikawa[39,40] reported more detailed studies of the temperature dependence of the (1/2,0) peak intensity, including a correction for the DW factor. These studies gave $\beta_1 \sim 0.89$, higher than the prediction for the Ising model (0.78–0.8) and the Heisenberg model (0.81), and below the mean-field value of 1. Consequently, no clear classification could be discerned from these measurements, raising the question of the surface sensitivity of LEED with respect to the temperature dependence of surface spin ordering.

We have recently demonstrated the high sensitivity of the new technique of metastable $2\,{}^3S$ helium-atom (He*) diffraction to surface antiferromagnetic ordering.[41–45] The de Broglie wavelength of these atoms at thermal kinetic energies is compatible with surface diffraction, and the classical scattering turning points occur at 3–4 Å in front of the crystal surface. Consequently, this technique is exclusively surface sensitive. Moreover, in contrast to LEED, it does not suffer from limitations imposed by surface charging effects. Our recent measurements on several crystalline rods from NiO ingots, obtained from Commercial Crystal Laboratories, Inc., have consistently shown a (2×1) surface electron-spin structure and a surface Neél temperature of 529 K, which is

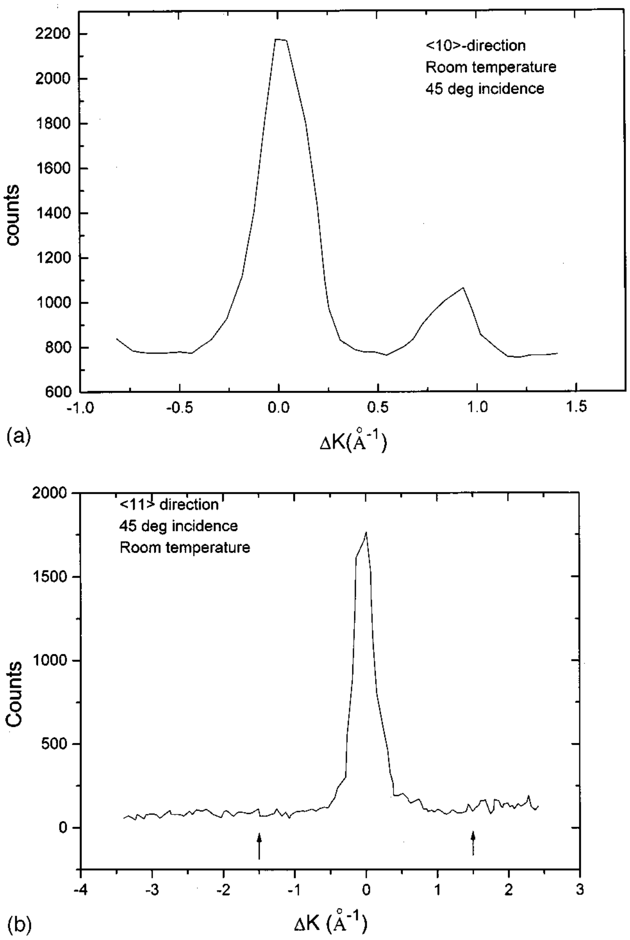

FIG. 1. He* diffraction spectra along (a) the ⟨10⟩ direction, (b) the ⟨11⟩ direction.

higher than the bulk value of 523.6 K. Figures 1(a) and 1(b) show He* diffraction spectra measured at room temperature along the ⟨10⟩ and ⟨11⟩ surface symmetry directions, respectively. The presence of $\frac{1}{2}$-order peaks along the ⟨10⟩ direction, and their absence along the ⟨11⟩ direction, establishes the fact that the periodicity of the surface electron-spin ordering is 2×1. Furthermore, analysis of the temperature dependence of the measured sublattice magnetization reveals a crossover behavior consistent with the class of the anisotropic extraordinary transition of the semi-infinite Heisenberg model,[46] whose critical behavior is very similar to that of the semi-infinite Ising model.[27]

Previous studies of the surface magnetic critical behavior of the $3d$ transition-metal surfaces Ni(001) and Ni(110) (Refs. 47 and 48) reported a behavior consistent with an ordinary transition. Several experimental studies of the surface of the $4f$ ferromagnet Gd have reported an enhanced surface magnetic transition temperature.[49–51] Evidence of a 15 K enhancement on polycrystalline Gd was first reported by Rau and Eichner using the technique of electron-capture spectroscopy (ECS).[49] Weller *et al.*, using SPLEED and magneto-optic Kerr effect techniques, subsequently reported a T_c^s enhancement of about 22 K for crystalline films grown on W(100),[50] but the reported critical behavior was complicated by an anomalous peak in the surface magnetization above T_c^b, which they attributed to a possible antiferromagnetic coupling to the bulk. Recently, further studies of this system,[51] employing SPSES and SPPES, reported T_c^s enhancement of up to 60 K, and revealed the presence of a component in the surface magnetization normal to the surface; the anomalous peak appears only in the component parallel to the surface, which was found to be oriented ferromagnetically with respect to the bulk magnetization. These complicating effects, however, prevented a clear investigation of the nature of the critical behavior. Another $4f$ system whose magnetic critical behavior was studied is Tb(0001).[52] It was found that the surfaces of thick films of Tb underwent a Curie transition at temperatures higher than the Neél and Curie temperatures of its bulk; moreover, the critical behavior of this transition consisted of that of the semi-infinite anisotropic Heisenberg system.

In Sec. II we discuss the principles of elastic scattering of He* atoms from magnetic surfaces, and explain how it leads to diffractive scattering from an ordered surface spin lattice. In Sec. III we present the details of the experimental facility and procedures. Section IV is devoted to establishing the relation between the intensities of the magnetic diffraction peaks and the corresponding sublattice magnetization; the details of the derivation, using the eikonal approximation, are given in Appendix A. In Sec. V, for the sake of completeness, we review the subject of magnetic critical behavior at surfaces and present in more detail the three classes of transitions that may occur, namely the ordinary, special, and extraordinary transitions, as well as the crossover function of Binder and Landau. The results of a configuration-interaction cluster calculation of the surface electronic structure of NiO(001) are presented in Sec. VI and used to evaluate the single-site magnetic anisotropy at the surface Ni^{+2} sites. We show that the results of the cluster calculations do not rule out either the possibility of enhancement of the magnetic superexchange coupling in the surface layer, as advocated recently by Sawatzky and co-workers,[53] or its suppression as proposed by de Graaf *et al.*[54] In Sec. VII we present the experimental data and discuss the ramifications of the recent results of a Schwinger-boson mean-field (SBMF) calculation by Murthy and Sharma.[55] These results, together with our experimental results, favor a scenario advocating a suppression of J_s.

II. ELASTIC SCATTERING OF He* BEAMS FROM MAGNETIC SURFACES

The lowest-lying excited state of atomic He is a metastable triplet $2\ ^3S$, with an excitation energy of 19.8 eV. It has the longest known lifetime of any atomic metastable state, $\sim10^4$ sec,[56–58] since spontaneous decay to the ground state must involve a two-photon transition and a spin-flip. The second lowest excited state of He is a metastable singlet $2\ ^1S$ with an excitation energy of 20.6 eV and a lifetime of 2×10^{-2} sec.[56–58] However, the techniques employed in the present work are based solely on the properties of the triplet metastable state; hereafter, we shall refer to it as the metastable state, denoted as He*. Moreover, since He* atoms at thermal energies travel with a velocity of about 1.7 km/sec, the transit time from source to sample over a typical distance of $\simeq$1 m is less than a millisecond, much shorter than its lifetime.

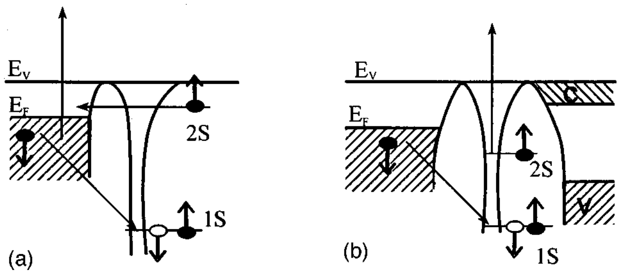

FIG. 2. (a) Resonance ionization/Auger, (b) Penning ionization neutralization process.

Although the 2 ^3S state of helium is very long-lived in vacuum, it readily decays to the ground state upon impact with atoms, molecules, and most surfaces. Conrad *et al.* measured survival probabilities 10^{-3}–10^{-6} for thermal energy He* atoms incident on clean metal surfaces, and 10^{-4} on insulator surfaces.[59]

A. Decay channels

There exist two predominant interaction channels that allow a He* atom to decay to its ground state as it approaches a surface: resonance ionization/Auger neutralization and Penning deexcitation.[59–62]

1. Resonance ionization/Auger neutralization process (RIAN)

This process, shown in Fig. 2(a), takes place when the excited He 2s orbital is degenerate with an unoccupied local density of surface electronic states. In that case, as the He* atom approaches the surface, it is first ionized by tunneling of the 2s electron into an available degenerate empty surface state. The resulting He$^+$ ion continues to travel towards the surface, where it is neutralized through an Auger process in which an electron from the surface with appropriate spin orientation fills the 1s hole of the He atom. The energy released in this process is imparted to a second surface electron which may be ejected from the surface if it has sufficient momentum along the surface normal.

2. Penning ionization (or Auger deexcitation) process

This process, shown in Fig. 2(b), prevails when the excited He 2s electron state is not degenerate with unoccupied surface states, but is degenerate with occupied states or lies in an electronic energy gap. Under such conditions, tunneling is inhibited. The decay then occurs via an Auger process involving a surface electron, with the appropriate spin orientation, and the 2s He* electron. In this process the surface electron fills the 1s He hole and the energy released is taken up by the 2s electron.

The escape probability of the ejected electron is higher for Penning deexcitation, because electrons emitted in RIAN can be reflected by the surface potential barrier. The most probable distances at which these processes occur have been measured.[63] Resonance ionization takes place 5–10 Å from the surface, and Auger neutralization takes place 2–3 Å from the surface. Penning deexcitation also takes place 5–10 Å from the surface. Note that deexcitation processes involving internal spin-flips of the 2s electron (i.e., converting the triplet into a singlet configuration) are energetically unfavorable and require high-order processes because the excitation energy of the singlet is almost 1 eV greater than that of the triplet.

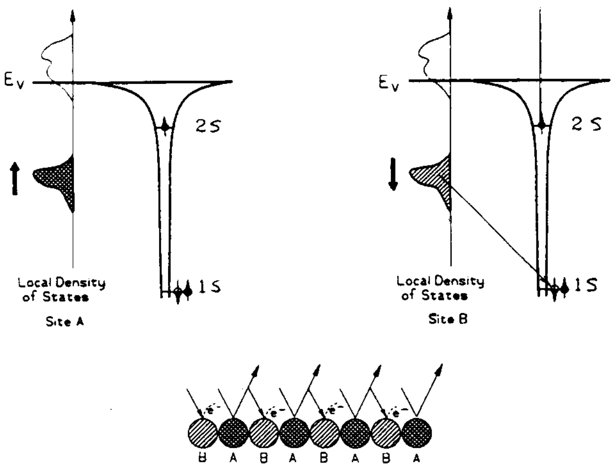

FIG. 3. Spin-dependent enhancement of the local survival probability of a He* beam.

B. Selection rules and magnetic diffraction

When the 2s He* electron state lies within the energy gap of a magnetic insulator, only Penning deexcitation can take place. If we take the polarization of the He* atom to be ''up,'' then the Pauli exclusion principle requires the spin polarization of the surface electron involved in the Auger deexcitation process to be ''down.'' Therefore, only surface electrons with ''down'' spin polarization can contribute to this decay process. The corresponding matrix element can be expressed as

$$\mathcal{M}_{\mathrm{Aug}}=\langle\phi_{1s\downarrow}\mathbf{k}'_{\uparrow}|W(r_1-r_2)|\mathbf{k}_{\downarrow}\phi_{2s\uparrow}\rangle\equiv\mathcal{M}^{k\downarrow 2s\uparrow}_{1s\downarrow k'\uparrow}, \qquad (1)$$

where $W(r_1-r_2)$ is the screened Coulomb interaction between the surface electron, in state $\mathbf{k}_{\downarrow}$, and the He* 2s electron in state $\phi_{2s\uparrow}$: $\phi_{1s\downarrow}$ and $\mathbf{k}'_{\uparrow}$ are the final states.

Thus, the survival probability will depend on the *relative orientations* of the spins of the He* 2s electron and the local surface electron: a He* atom will be more likely to survive scattering if its spin orientation is parallel to the local surface electron spins, but will be more likely to decay to the ground state if the spins are antiparallel. Accordingly, if the orientations of the local moments on the surface are arranged periodically, the beam attenuation should exhibit a periodic modulation, which will be reflected in the diffraction pattern of the elastically scattered He* atoms. Thus, diffractive He* scattering reflects the surface spin ordering as well as the geometric surface structure.

As an example, we consider what will happen to a beam of metastables incident upon the ideal antiferromagnetic surface shown in Fig. 3. By *ideal* we mean that all of the valence electrons on the sites in sublattice A have the same spin orientation, while all of the valence electrons on the sites in sublattice B have antiparallel spin orientation. Let us also assume that the incident metastable beam is polarized parallel to the spin orientation of the A sublattice. Then all of the metastables that strike B sites will decay to the ground state, whereas metastables that strike A sites will survive the scattering event and yield a diffraction pattern reflecting the periodicity of the surface spin-ordering. This process is analogous to light scattering from a reflective grating: light which strikes the slits in the grating is lost, while the reflected light is diffracted. If the incident metastable beam is unpolarized, some metastables will be elastically scattered from both sublattices, and the resulting diffraction pattern will reflect the periodicity of the surface spin-ordering. However, such an experiment will not yield information about the absolute spin direction of the lattice.

Of course, on a real antiferromagnetic surface, majority and minority spins will be present at all sites, and thus the metastable beam will experience attenuation at all sites. However, if the surface sites have a net spin, the attenuation of the He* beam will be periodically modulated, and the resulting diffraction pattern will again reflect the periodicity of the surface spin-ordering.

III. EXPERIMENTAL SETUP AND PROCEDURES

Our experimental facility is comprised of two main components: a monochromatic He* beam generator and an ultrahigh-vacuum (UHV) scattering chamber. The first stage of the beam generator is a monochromater, based on a nozzle/skimmer assembly, which produces a monoenergetic beam of ground-state helium atoms with energy resolution better than 1%. The second stage is the He* exciter,[64] which is based on a coaxial excitation geometry. It is comprised of a high current electron gun of the Pierce type, equipped with a specially designed hemispherical matrix cathode, and a three-stage electrostatic quadrupole for electron-beam axial confinement. The details of the design and operation have been presented in Ref. 64. Beam intensities of about 10^5 He* atoms/s at the sample surface were achieved in the present measurements.

The UHV chamber houses a detector consisting of a channeltron electron multiplier and an angle-resolving aperture. The detector is exclusively sensitive to He* atoms, since it registers electron emission events associated with He* deexcitation. It was mounted on a single-axis goniometer attached to a 33.5 cm D flange, which also supports a sample manipulator equipped with *XYZ* motions, polar and azimuthal rotations, and a sample heater. The rotation axis of the goniometer coincides with the polar rotation axis of the manipulator. The chamber is also equipped with traditional diagnostic, monitoring, and sample preparation capabilities such as LEED/Auger spectrometers, residual gas analyzer, and a specially designed retractable UHV crystal cleaver.

All of the data were obtained from NiO(100) surfaces freshly cleaved in vacuum, with a background pressure less than 10^{-10} Torr with the He beam turned off. The NiO samples used in these experiments were oriented and cut into rods approximately $8\times3\times4$ mm, with the long axis parallel to the $\langle 100\rangle$ direction, and with transverse cleavage grooves spaced 2 mm apart. Each rod yielded two cleaves, on average. Silver conducting epoxy was used to attach an iron-constantan thermocouple to the sides of the rods at the location of the last cleavage groove. Scans were taken at 2 K increments near the bulk Néel temperature, and at larger increments closer to room temperature. The temperature was not allowed to vary more than ±1 K during any scan. The thermocouple controller (Omega model 199) is factory-calibrated to an ice-water standard for iron-constantan thermocouples. Its calibration was checked independently, using ice-water and boiling water baths, and was found to be accurate to within 1 K. Measurements of the diffraction intensities consistently yielded a surface Neél temperature of 529 K for all the successively cleaved surfaces, irrespective of their distance from the affixed thermocouple. After the first cleave the sample surface was at about 2.0–2.5 mm away from the thermocouple, and after the second and final cleave, the thermocouple was located precisely at the cleaved surface. The bulk Neél temperature was determined by measuring the specific heat of several bulk samples, taken from the crystal rods, as a function of temperature with a Perkin-Elmer model DSC7 differential scanning calorimeter. Figure 4 shows that the anomaly in the specific heat associated with the bulk Neél transition occurs at $T_N^b=523.6\pm0.2\,\mathrm{K}$.

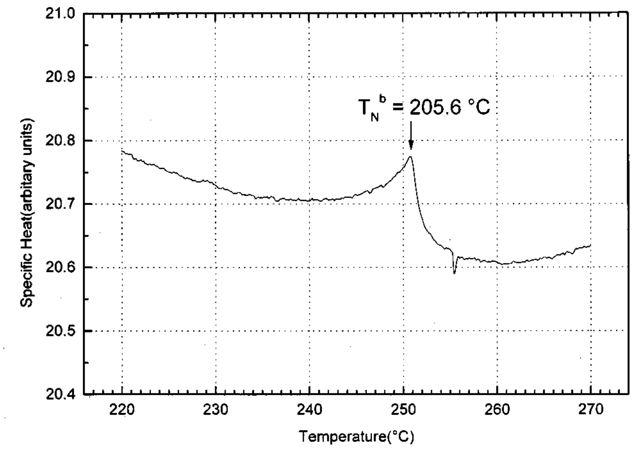

FIG. 4. Temperature dependence of the bulk specific heat showing the anomaly associated with the Neél transition at 523.6 K.

Initially, we performed several experiments to rule out the possibility that our detector was recording photons. When the electron-beam energy was reduced below the threshold for excitation to the triplet He* state (i.e., below 19.8 eV), while the heating current of the matrix cathode was maintained at its normal operating value, the channelron detector output dropped to the dark current level (<0.2 counts/sec), ruling out photon contributions from the matrix cathode filament leads. We avoided the need for a singlet quenching lamp and excluded contributions from radiative excitation processes, by holding the electron-beam energy at 20.3 eV, corresponding to the ^2P peak in the triplet excitation cross section, but below the threshold for singlet excitation, 20.6 eV. It should also be noted that when the cleaved NiO crystal surface was allowed to remain in the vacuum long enough for surface contamination to become important, the diffraction peaks were greatly attenuated, further evidence that our recorded signals were indeed caused by diffraction of He* atoms, and not by photons. Furthermore, we observed that reversal of the relative directions of the helium and electron beams in the exciter (i.e., from parallel to antiparallel), thus changing the energy and therefore the de Broglie wavelength of the He* atoms, alters the diffraction beam spacings. Note also that no He^+ ions can be produced below the threshold of 24 eV for ionization by electron impact. Recent time-of-flight measurements of the velocity distribution in the metastable He beam generated with 20.3 eV excitation energy confirmed the absence of photons.

IV. RELATIONSHIP BETWEEN MAGNETIC PEAK INTENSITIES AND SUBLATTICE MAGNETIZATION

A. The dissipative potential and the differential reflection coefficient in the eikonal approximation

The dissipative nature of the scattering of He* beams from the AF surfaces of NiO is taken into account by introducing a complex scattering potential whose imaginary part corresponds to the beam attenuation during scattering. This, in turn, can be separated into two components: (i) a spin-independent part which can be regarded as a constant background,

$$V_0 = C_0 \mathcal{M}_{\mathrm{Aug}} \mathcal{D}_0, \tag{2}$$

where $\mathcal{M}_{\mathrm{Aug}}$ is the Auger matrix element defined in Eq. (1), pertinent to the PI decay channel, $\mathcal{D}_0$ is an average background local density of surface electronic states available for the PI decay, and the constant C_0 encompasses all the remaining constants; (ii) a spin-dependent second part, ΔV^S, which has the periodicity of the magnetic lattice. Taking advantage of the fact that in this case the survival or decay of a He* atom depends on the relative orientation of the spin $\mathbf{\Sigma}$ of its $2s$ electron with respect to the local electron spin $\mathbf{S}(\mathbf{R})$ of a surface magnetic ion at $\mathbf{R}$, we can write the spin-dependent component of the imaginary potential in terms of the averaged scalar product of the spins $\langle \hat{\mathbf{\Sigma}} \cdot \hat{\mathbf{S}}(\mathbf{R}) \rangle$ as

$$\Delta V^S(\mathbf{r}) = C_0 \mathcal{M}_{\mathrm{Aug}} \mathcal{D}[S(\mathbf{R});z] \langle \hat{\mathbf{\Sigma}} \cdot \hat{\mathbf{S}}(\mathbf{R}) \rangle, \tag{3}$$

where $\mathcal{D}[S(\mathbf{R});z]$ is the spin-dependent surface local density of states. We use the convention $\mathbf{r} \equiv (\mathbf{R}, z)$, where $\mathbf{R}$ is a vector parallel to the surface plane. Since in this picture both spins enter as noninteracting parameters and not as dynamical variables, we have $\langle \hat{\mathbf{\Sigma}} \cdot \hat{\mathbf{S}}(\mathbf{R}) \rangle = \langle \hat{\mathbf{\Sigma}} \rangle \cdot \langle \hat{\mathbf{S}}(\mathbf{R}) \rangle$, and obtain

$$\begin{aligned}\Delta V^S(\mathbf{r}) &= C_0 \mathcal{M}_{\mathrm{Aug}} \mathcal{D}[S(\mathbf{R});z] \{ \langle \hat{\Sigma}_z \rangle \langle \hat{S}_z(\mathbf{R}) \rangle \\ &\quad + \tfrac{1}{2} [\langle \hat{\Sigma}^+ \rangle \langle \hat{S}^-(\mathbf{R}) \rangle + \langle \hat{\Sigma}^- \rangle \langle \hat{S}^+(\mathbf{R}) \rangle] \} \\ &= C_0 \mathcal{M}_{\mathrm{Aug}} \mathcal{D}[S(\mathbf{R});z] \langle \hat{\Sigma}_z \rangle \langle \hat{S}_z(\mathbf{R}) \rangle. \end{aligned} \tag{4}$$

We can now write $\langle \hat{\Sigma}_z \rangle = \frac{1}{3}$ and write the total imaginary part of the potential as

$$V_I(\mathbf{r}) = \begin{cases} -iV_0 \{ 1 + (\frac{1}{3}) \xi(\mathbf{R}) \langle \hat{S}_z(\mathbf{R}) \rangle \} & \text{if } z_0 > z > 0, \\ 0 \quad \text{otherwise}, \end{cases} \tag{5}$$

where $\xi(\mathbf{R}) = \{ \mathcal{D}[S(\mathbf{R});z] / \mathcal{D}_0 \}$, and z_0 is an effective range above the surface. Obtaining an expression for the imaginary part of the potential in terms of the averaged sublattice spin $\langle \hat{S}_z(\mathbf{R}) \rangle$ allows us to introduce its temperature dependence, which may be expressed in terms of a surface critical exponent β_1 as

$$\langle \hat{S}_z(\mathbf{R}) \rangle = s_0 \left(\frac{T_N^s - T}{T_N^s} \right)^{\beta_1}, \tag{6}$$

where s_0 is the effective sublattice spin at 0 K, which is less than the value $s=1$ due to the zero energy fluctuations, T_N^s is the surface Neél temperature, T is the surface temperature, and β_1 is a surface critical exponent. Then we can express $\Delta V^S(\mathbf{r})$ as

$$\Delta V^S(\mathbf{r}) = \tfrac{1}{3} C_0 \mathcal{M}_{\mathrm{Aug}} \mathcal{D}[S(\mathbf{R});z] s_0 \left(\frac{T_N^s - T}{T_N^s} \right)^{\beta_1}. \tag{7}$$

As shown in Appendix A 1, by considering the simple case of a hard corrugated wall with dissipation we obtain the following expression for the scattering wave function for the He* beam:

$$\Psi(\mathbf{r}) = A \exp\left\{ i[\mathbf{K} \cdot \mathbf{R} + k_z \zeta(\mathbf{R})] - \frac{1}{\hbar v_z} \int_{z_0}^{z} V_I(\mathbf{R}, z') dz' \right\},$$

where $\zeta(\mathbf{R})$ is the corrugation shape function and $V_I(\mathbf{R},z')$ is the dissipative imaginary potential of Eq. (5). Next, by expressing the differential reflection coefficient in terms of the transition operator $\hat{T}$,[65–67]

$$\frac{d^2 R}{\partial E\, \partial \Omega} = \frac{L^4 M^2}{8\pi^3 \hbar^5} \frac{v}{v_{iz}} \int_{-\infty}^{\infty} \exp\left(-i \frac{Et}{\hbar} \right) \times \langle \hat{T}^\dagger_{\mathbf{p} \leftarrow \mathbf{p}_i}(0) \hat{T}_{\mathbf{p} \leftarrow \mathbf{p}_i}(t) \rangle dt,$$

and using Eq. (A5) for the scattering wave function in the eikonal approximation, we arrive, after a lengthy derivation given in Appendix A 2, at an expression for the diffraction amplitude, $\tilde{\mathcal{A}}_{\mathbf{G}}$, in terms of the periodic dissipative potential associated with the sublattice magnetization, namely,

$$\tilde{\mathcal{A}}_{\mathbf{G}} = \frac{1}{\Omega} \int_{\mathrm{u.c.}} d\mathbf{R} \exp\left\{ i[\mathbf{G} \cdot \mathbf{R} + q_z \zeta(\mathbf{R})] - W - \frac{\alpha}{\tilde{q}_z} [1 - (\tfrac{1}{3}) \xi(\mathbf{R}) \langle \hat{S}_z(\mathbf{R}) \rangle] \right\},$$

where Ω is the area of the surface primitive mesh and W is the Debye-Waller factor. α and $\tilde{q}_z$ are defined in Appendix A 2.

B. A simple model for He* diffraction intensities from the NiO(100) surface

As we have presented in Sec. I, He* diffraction spectra demonstrate that NiO(001) exhibits a 2×1 spin periodicity. Moreover, previous He^0 diffraction experiments have consistently reported a first-order diffraction peak intensity equal to about a tenth of the specular peak intensity, leading to an effective surface corrugation <0.14 Å.[68–71] Therefore, for the sake of simplicity, we shall neglect the corresponding hard-wall corrugation in our analysis, and set $\zeta_0(\mathbf{R}) = 0$. We now introduce the 2×1 magnetic periodicity by setting

$$\begin{aligned}\frac{\alpha}{3\tilde{q}_z} \xi(\mathbf{R}) \langle \hat{S}_z(\mathbf{R}) \rangle &= \frac{\alpha}{3\tilde{q}_z} s_0 \left(1 - \frac{T}{T_N} \right)^{\beta_1} \cos(\pi X/a) \\ &= B \cos(\pi X/a) \end{aligned} \tag{8}$$

along one of the two equivalent[10] directions. From Eq. (A19) we obtain the amplitude of the half-order magnetic diffraction peak as

$$\mathcal{A}_{(\pi/a,0)}=\frac{1}{2a}\exp\left[-W-\frac{\alpha}{\tilde{q}_z}\right]\int_{-a}^{a}dX\exp\left\{i\frac{\pi X}{a}+B\cos(\pi X/a)\right\}$$

$$=\frac{1}{\pi}\exp\left[-W-\frac{\alpha}{\tilde{q}_z}\right]\int_{0}^{\pi}dY\cos(Y)\exp\{B\cos(Y)\}$$

$$=\exp\left[-W-\frac{\alpha}{\tilde{q}_z}\right]I_1(B), \tag{9}$$

where W is the Debye-Waller factor, $\alpha/\tilde{q}_z$ is the effective attenuation constant due to decay, and $I_1(x)$ is the modified Bessel function of order 1 given by

$$I_1(x)=\frac{1}{\pi}\int_0^{\pi}dx\cos(x)\exp[x\cos(x)]=\frac{x}{2}\sum_{k=0}^{\infty}\frac{(x/2)^{2k}}{k!(k+1)!}.$$

Note that the first term in the expansion corresponds to the expression obtained using the Born approximation:

$$\mathcal{A}^{\mathrm{Born}}_{(\pi/a,0)}=\frac{\alpha s_0}{6\tilde{q}_z}\exp\left[-W-\frac{\alpha}{\tilde{q}_z}\right]\left(1-\frac{T}{T_N}\right)^{\beta_1}. \tag{9$'$}$$

Thus, in keeping all the higher terms, we expect the eikonal approximation to yield a more accurate description of the scattering process.

Similarly, the specular peak intensity is given by

$$\mathcal{A}_{(0,0)}=\frac{1}{2a}\exp\left[-W-\frac{\alpha}{\tilde{q}_z}\right]\int_{-a}^{a}dX\exp\{B\cos(\pi X/a)\}$$

$$=\frac{1}{\pi}\exp\left[-W-\frac{\alpha}{\tilde{q}_z}\right]\int_{0}^{\pi}dY\exp\{B\cos(Y)\}$$

$$=\exp\left[-W-\frac{\alpha}{\tilde{q}_z}\right]I_0(B), \tag{10}$$

where $I_0(x)$ is the modified Bessel function of order 0, and is given by

$$I_0(x)=\sum_{k=0}^{\infty}\frac{(x/2)^{2k}}{(k!)^2}.$$

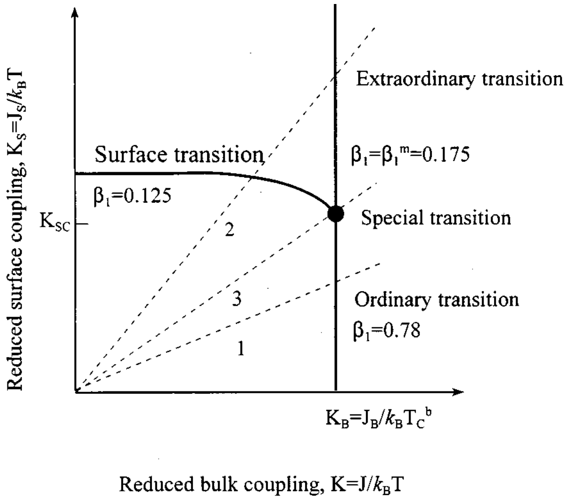

FIG. 5. Phase diagram for a semi-infinite ferromagnetic Ising system on a simple cubic lattice.

V. MAGNETIC CRITICAL BEHAVIOR AT SURFACES

There have been extensive theoretical and computational studies of the magnetic critical behavior at surfaces over the past 25 years.[24,25] These studies demonstrated that the universality classes associated with surface magnetic transitions are strongly dependent on the relative strengths of surface magnetic coupling and bulk, the surface magnetic anisotropy,[69] and surface symmetry. For the case of antiferromagnetic phases, the universality class will also depend on the surface orientation.[72] In order to illustrate these concepts, we shall consider the case of an Ising-like system, which has a lower critical dimension $d^*=1$. Figure 5 shows the phase diagram of a semi-infinite ferromagnetic Ising model in the mean-field limit, in the absence of external fields. The phase diagram is depicted in terms of reduced exchange couplings $K_b=J_b/kT$, and $K_s=J_s/kT$, where T is the temperature and J_b, J_s are the effective bulk and surface exchange couplings, respectively. Consequently, in Fig. 5 the origin corresponds to infinite temperature. Paths 1, 2, and 3 represent the expected behavior when the effective surface exchange coupling J_s is less than, greater than, or equal to a critical value (J_s^c), respectively. When $J_s<J_s^c$ (path 1), the effective field at the surface is less than that in the bulk, suggesting (naively) that the surface might order at a *lower* temperature than the bulk. However, in this case, the bulk field is strong enough to force the surface to order passively at the bulk critical temperature, T_c^b. This critical behavior, coined an *ordinary transition*, is characterized by a critical exponent for the surface sublattice magnetization $\beta_1=0.78$–0.8.[27–29] In the language of renormalization-group theory, ''the (running) surface coupling is driven to the stable fixed point $J_s=0$ corresponding to the universality class of the ordinary transition.''[73] When $J_s=J_s^c$ (path 3), the surface and bulk effective fields are comparable, and the two systems order independently at T_c^b. This surface transition, which independently coincides with the bulk critical temperature, is called the *special transition*, and is characterized by the critical exponent $\beta_1=\beta_1^m=0.175$. In renormalization-group theory, the special transition is an unstable fixed point.[73]

Finally, in the case $J_s>J_s^c$ (path 2), the surface effective field is stronger than that of the bulk, and the surface orders at $T_c^s>T_c^b$, undergoing a pure ''surface transition.'' This is a purely 2D transition since the bulk is still in a paramagnetic state with a zero field, and it should therefore be characterized by the critical exponent $\beta_1=0.125$ corresponding to a 2D Ising system. As the temperature of the system is lowered to the bulk critical temperature, we again have two independent critical fields, and as such this behavior is described by the critical exponent relevant to the multicritical point, $\beta_1=0.175$. In renormalization-group theory, one says that the surface ''is driven to $J_S=\infty$, again a stable fixed point, corresponding to the universality class of the extraordinary transition.''[73]

Binder and Landau performed extensive Monte Carlo simulations of a semi-infinite Ising system on a simple cubic lattice, in order to study the critical behavior of its surface as a function of J_s/J_b.[27] These studies revealed several important aspects of the surface critical behavior. First, for values of $J_s/J_b<1$ they consistently obtained a critical exponent of the magnetization $\beta_1=0.78$, corresponding to the ordinary transition; more accurate values, $\beta_1\simeq 0.8$, were obtained recently.[28,29] Second, for values of $1<J_s/J_b\leqslant 1.7$ they obtained what seemed to be a continuous decrease of β_1 to values below $\beta_1=0.125$ of the two-dimensional Ising model. Recognizing that this behavior is due to a crossover associated with the multicritical point at the critical value J_s^c, and introducing a 2D Ising transition at a temperature $T_c^s>T_c^b$, with $\beta_1=0.125$, they obtained a critical value $J_s^c\simeq 1.52J_b$. Moreover, they derived a *crossover scaling function* $\tilde{m}_1^{\mathrm{SF}}(x)$, in the neighborhood of the multicritical point, which describes the crossover from the surface transition to the extraordinary transition, for temperatures less than the bulk critical temperature ($T<T_c^b$):

$$m_1=\tilde{m}_1^{\mathrm{SF}}(x)\left(\frac{T_c^b}{T}-1\right)^{\beta_1^m}, \tag{11}$$

where the parameter x describes the dependence on J_S/J_s^c and $(T_c/T-1)$:

$$x=\frac{|J_s/J_s^c-1|}{(T_c^b/T-1)^{\phi}} \tag{12}$$

with the crossover exponent $\phi=0.56$. Binder and Landau then demonstrated that all their simulation data for $J_s/J_b \gtrless J_s^c$ collapse on two branches by plotting the reduced surface magnetization $B/(T_N^b/T-1)^{0.175}$ against the crossover scaling variable, $|J_s/J_{\mathrm{sc}}-1|/(523/T-1)^{\phi}$.[27] The upper branch corresponds to $J_s/J_b>J_s^c$ (path 2 in Fig. 5), while the lower branch corresponds to $J_s/J_b<J_s^c$ (path 1 in Fig. 5). They also indicate that data corresponding to the multicritical point (path 3 in Fig. 5) would fall on a horizontal line in this diagram. These results are universal in the sense that they hold for all anisotropic three-dimensional magnetic systems near T_c^b.

According to the well-known Hohenberg-Mermin-Wagner theorem,[74,75] the lower critical dimension for the appearance of spontaneous order is $d_*=2$ for systems with continuous symmetries, rather than $d_*=1$ for the Ising systems ($n=1$). Consequently, the extraordinary, surface, and special transitions should not take place for systems with continuous $O(n)$, $n>1$ symmetries, such as the Heisenberg system. However, the continuous symmetry of the 3D bulk may be broken at the surface due to the presence of surface anisotropies which are inhibited in the bulk due to its inherently higher symmetry. These surface anisotropies may arise, especially if the interactions are short-range, in which case an easy-magnetization axis may be favored at the surface. Under these conditions, a surface transition akin to the Ising-type may take place. Accordingly, there should be a multicritical point and, hence, anisotropic analogs of the special and extraordinary transitions. Yet, one expects that these transitions would belong to a different universality class from those associated with the Ising system. The multicritical transition associated with such anisotropies was investigated, in the generalized case of d dimensions and $O(n)$ symmetry, by Diehl and Eisenriegler,[46] using renormalization-group methods; they labeled it the ''anisotropic special'' transition. It is interesting to note that for the 3D case they obtain a crossover exponent of $\simeq 0.57$, surprisingly close to that of the Ising system quoted above.

The NiO system has isotropic first- and second-neighbor exchange couplings. Moreover, because of the octahedral symmetry in the bulk, the spin-orbit-coupling site energies are isotropic and hence there is no site anisotropy except for very weak dipolar interactions, as well as the slight distortions from the cubic structure that accompany the AF phase. Although these anisotropies determine the magnetization direction, their magnitude is so small, $D_1\simeq 0.1$ meV and $D_2 \simeq 0.006$ meV, that they are not expected to play a decisive role in determining the bulk Neél transition, $T_N^b=523.6$ K. The NiO spin system in the bulk may, therefore, be classified as a Heisenberg system. However, as we shall show below, the reduction in symmetry at the surface gives rise to an appreciable uniaxial single-site anisotropy that places the critical behavior of the surface in the anisotropic 3D, $n=3$ universality class.

VI. SOME RELEVANT PROPERTIES OF NiO(001)

Several experimental studies of the structure of the NiO(001) surface, employing He^0 scattering, have been reported in the literature.[68–71] All these studies showed that this surface does not undergo any reconstruction. The most recent work was reported by the Göttingen group, and included measurement of the surface-phonon dispersions.[69,71] The reported results confirmed the absence of any sign of reconstruction over a wide temperature range and no discernable effect on the surface-phonon dispersions as the surface temperature went from well below to well above the Neél transition. Moreover, diffraction measurements showed that the effective surface corrugations are less than 0.14 Å.[68]

A. Electronic structure and He* scattering

The ground state of a free Ni^{2+} ion, with $3d^3$ electrons, has a ^{3}F configuration. In bulk NiO, the ^{3}F ground state is split into a nondegenerate $^3A_{2g}$ ground state and two threefold-degenerate excited states $^3T_{2g}$ and $^3T_{1g}$ by the octahedral symmetry of the ligand, or crystal, field. The $^3A_{2g}$ ground state has the electron configuration $(t_{2g}^6e_g^2)$, while the $^3T_{2g}$ has the configuration $(t_{2g}^5e_g^3)$ and $^3T_{1g}$ has the configuration $(t_{2g}^4e_g^4)$ mixed with some $(t_{2g}^5e_g^3)$. In order to determine the energy splittings in the bulk and on the surface, we performed extensive electronic-structure calculations using Hartree-Fock states with configuration interaction for a cluster model. Similar calculations have been performed in the past, yielding exchange energies for NiO in good agreement with experimental values.[76,77] The results of these calculations are shown in Fig. 6. The energy splittings between the bulk $^3A_{2g}$ ground state and the $^3T_{2g}$ and $^3T_{1g}$ excited states are about 1.1 and 1.8 eV, respectively.

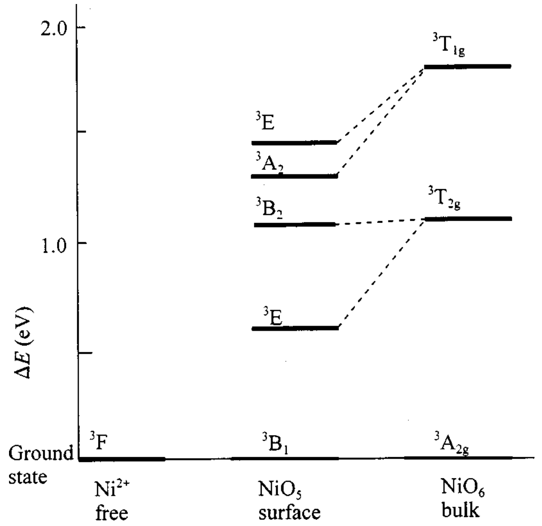

FIG. 6. Schematic of the electronic structure of Ni^{2+} in the free ion, NiO(001) surface, and NiO bulk.

The lowering of symmetry to $\mathcal{C}_{4v}$ at the NiO(001) surface leads to a ${}^3B_1$ ground state, with similar filling to the ${}^3A_{2g}$. The degeneracies of the two lowest excited states are partially removed with

$$
{}^3T_{2g}\rightarrow\begin{cases} {}^3E & \text{twofold} \quad (0.60 \text{ eV}) \\ {}^3B_2 & (1.10 \text{ eV}), \end{cases}
$$

$$
{}^3T_{1g}\rightarrow\begin{cases} {}^3A_2 & (1.30 \text{ eV}) \\ {}^3E & \text{twofold} \quad (1.44 \text{ eV}), \end{cases}
$$

where the numbers in parentheses are excitation energies from the ground states. The ${}^3B_2$ excited state corresponds to the excitation $3d_{xy}\rightarrow 3d_{x^2-y^2}$ and is not affected by the missing O^{2-} ion at the surface, whereas the ${}^3E$, which corresponds to $3d_{xz}\rightarrow 3d_{z^2}$ and $3d_{yz}\rightarrow 3d_{z^2}$ excitations, is lowered in energy. The configurations of the state splitting from ${}^3T_{1g}$ are more complicated.

Photoemission and inverse-photoemission measurements of the density of states for NiO(100) (Ref. 78) place the conduction-band edge, with d^9 configuration, at 4.3 eV above the top of the valence band. A schematic diagram of these results is presented in Figure 7. Since the valence-band edge is placed at about 5.5 eV below the vacuum level and has the d^8 configuration of the ground state, the excited d^9 configuration would then be placed at about 1.2 eV below the vacuum level,[79] as indicated in Fig. 7. Furthermore, these experiments show that the bottom of the unoccupied bulk $4sp$ band lies about 9.5 eV above the top of the valence band, or about 4 eV above the vacuum level. This is consistent with estimates of the bandwidth (W_s) by band-structure calculations of about 6 eV,[80] with $3/4W_s$ below the $(3d)^7 4s$ energy level. Since the tunneling of the He* $2s$ electron at the Ni^{2+} site would lead to a d^9 configuration, energy conservation would rule out the RIAN process, because the $2s$ level of the He* atom lies at 4.7 eV below the vacuum level. Even the shift and broadening of the He* $2s$ level due to admixing with the surface states would not lead to such a large energy shift, especially since NiO is an insulator with no image potential present.

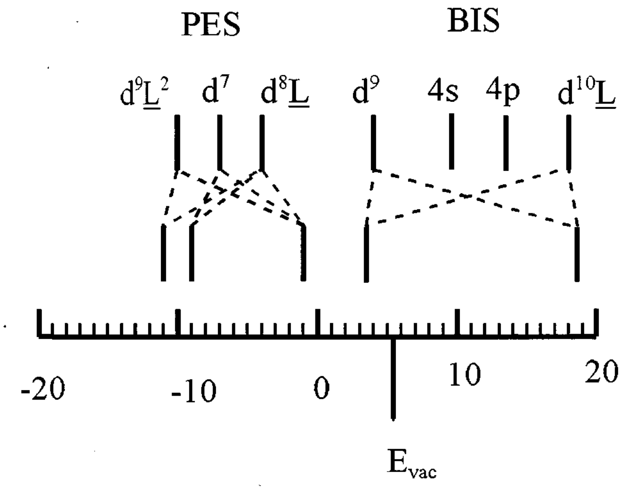

FIG. 7. Schematic of excited states of NiO, measured by photoemission and inverse photoemission (Ref. 66).

B. Magnetic coupling and anisotropies at the NiO(001) surface

The bulk magnetic exchange interactions and anisotropies in NiO have been extensively studied both experimentally and theoretically over the past 30 years. By contrast, their surface counterparts have only recently become the focus of a few theoretical investigations. Recently two contradicting theoretical studies on the surface superexchange interaction $J_{\mathrm{sup}}\equiv J_2$ have been reported. On the one hand, Pothuizen *et al.*[53] argued that J_{sup} in the late transition-metal oxides is strongly enhanced relative to its bulk value. They reason, using a model Hamiltonian, that the decrease in the crystal field at the surface leads to lower charge-transfer energy Δ, which in turn gives rise to an increase of J_{sup} by roughly a factor of 1.5 for all the transition-metal oxides considered. On the other hand, de Graaf *et al.*,[54] using a $\mathrm{Ni}_2\mathrm{O}_x$ cluster embedded in a Madelung potential of the rest of the crystal, argue that a decrease in the Ni coordination number leads to a decrease in J_{sup} that offsets the increase due to the reduction in the crystal field at the surface. They obtain an effective decrease in J_{sup} of about 20% with respect to the bulk value.

Moreover, although the single-site spin-orbit energy is isotropic in the bulk because of the octahedral symmetry, it will give rise to an appreciable single-site anisotropy at the surface, due to the reduction in symmetry to C_{4v}, a fact that has been consistently overlooked in the past. The Hamiltonian of the single-site anisotropy, $\mathcal{H}_{\mathrm{ssa}}$, is expressed to second order in the spin-orbit (SO) coupling as

$$
\mathcal{H}_{\mathrm{ssa}}=\lambda^2\sum_{ij} \Lambda_{ij}S_iS_j, \tag{13}
$$

where λ is the SO coupling parameter, S_i, $i=1,2,3$, are the Cartesian components of the spin, and the matrix Λ is given by

$$
\Lambda_{ij}=\sum_n{}' \frac{\langle 0|L_i|n\rangle\langle n|L_j|0\rangle}{E_n-E_0}. \tag{14}
$$

E_0 is the ground-state energy, L_i are the components of the orbital angular momentum, and n runs over the manifold of

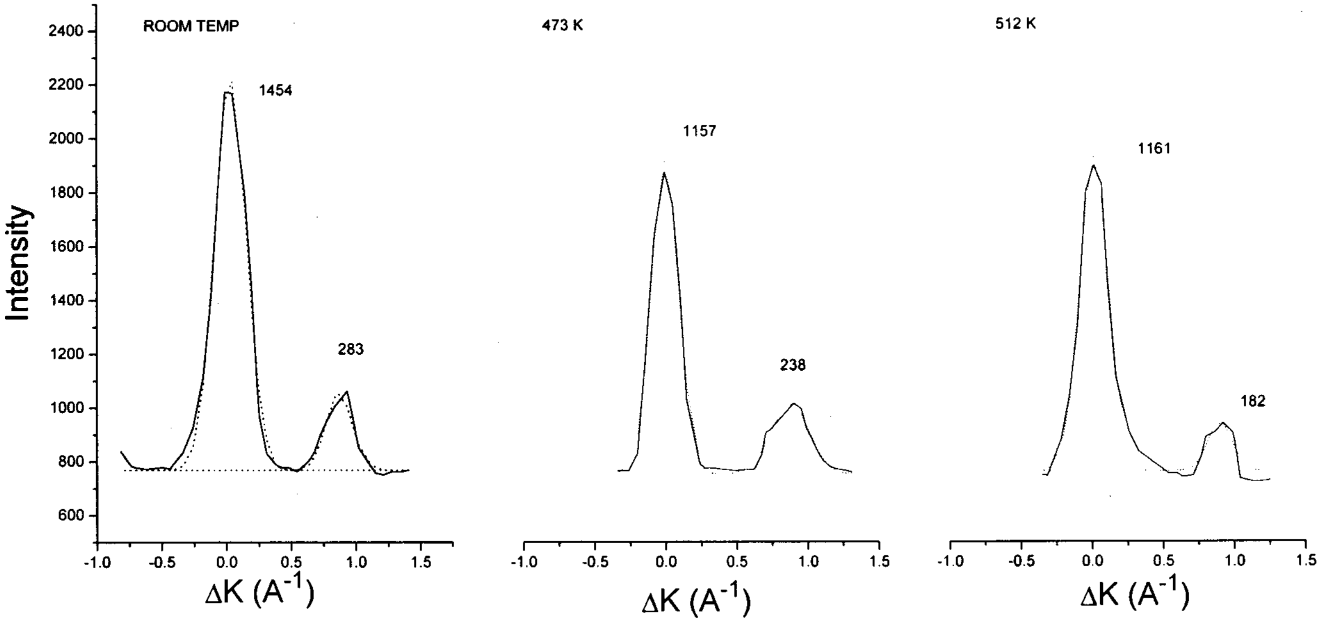

FIG. 8. He* diffraction spectra along the (10) direction at (a) room temperature, (b) 473 K, and (c) 512 K.

excited states originating from the $3d$ orbitals. For the present case $\mathcal{H}_{\rm ssa}$ can be written in the form

$$\begin{aligned}\mathcal{H}_{\rm ssa}=\lambda^2\{&\tfrac{1}{3}[\Lambda_{xx}+\Lambda_{yy}+\Lambda_{zz}]S(S+1)\\&+\tfrac{1}{3}[\Lambda_{zz}-\tfrac{1}{2}(\Lambda_{xx}+\Lambda_{yy})][3S_z^2-S(S+1)]\\&+\tfrac{1}{2}[\Lambda_{xx}-\Lambda_{yy}][S_x^2-S_y^2]\}.\end{aligned}\qquad(15)$$

Because of the octahedral symmetry in the bulk, $\Lambda_{zz}=\Lambda_{xx}=\Lambda_{yy}$ and the anisotropy energy vanishes to second order, with the first nonvanishing contribution coming in the fourth order. By contrast, the $\mathcal{C}_{4v}$ symmetry at the surface leads to $\Lambda_{zz}\equiv\Lambda_{\perp}\neq\Lambda_{xx}=\Lambda_{yy}\equiv\Lambda_{\parallel}$. Thus, apart from constant terms, we have $\Lambda_{\perp}$ and $\Lambda_{\parallel}$ such that the single-site anisotropy Hamiltonian at the surface $\mathcal{H}_{\rm ssa}^S$ is given by

$$\mathcal{H}_{\rm ssa}^{\rm S}=\lambda^2[\Lambda_{\perp}-\Lambda_{\parallel}]S_z^2=DS_z^2,\qquad(16)$$

where the z axis is taken perpendicular to the surface. The matrix elements Λ_{ij} calculated using the data for the surface electronic structure discussed in Sec. VI A and Eq. (14) give $\Lambda_{\parallel}-\Lambda_{\perp}=-1.36$. For Ni^{2+}, $\lambda=-325\,\mathrm{cm}^{-1}\approx 40\,\mathrm{meV}$,[81] which gives an estimate of $D\approx-2.5\,\mathrm{meV}$, so that $D/J_2^b\approx 0.13$.

VII. NiO(100): RESULTS AND DISCUSSION

In light of all the preceding considerations, we now turn to examining the measured data. We start with a comment on the apparent absence of the first-order diffraction peaks in Fig. 1. We attribute this to two factors. First, the scattered He* beam suffers an attenuation $\propto\exp[-2\alpha/\tilde{q}_z]$; this attenuation is greater for the first-order beams than for the $\frac{1}{2}$-order beams since $\tilde{q}_z$ is smaller for the former. Second, the intensities of the first-order peaks, measured by He^0 diffraction, are less than a tenth of the specular intensity, pointing to a very small surface corrugation for the NiO(001). Both of these factors could very well lead to extremely low intensities of the first-order peaks that are not discernible in the He* diffraction spectra. To determine the temperature dependence of the sublattice magnetization, we measured the intensity of the specular (0,0) and half-order (1/2,0) peaks along the ⟨10⟩ direction in the temperature range 300–536 K, i.e., from room temperature to above the bulk Néel temperature, 523 K. Figure 8 shows three typical scans along the ⟨10⟩ direction, at room temperature, 473 K, and 512 K. The intensity of the half-order peak is seen to decrease faster with temperature than that of the specular peak. Figure 9 shows the intensity of the surface (1/2,0)-order magnetic diffraction peak as a function of the surface temperature. The width of the points reflects the experimental uncertainty in the measured intensity. The solid curve is a least-square fit to the

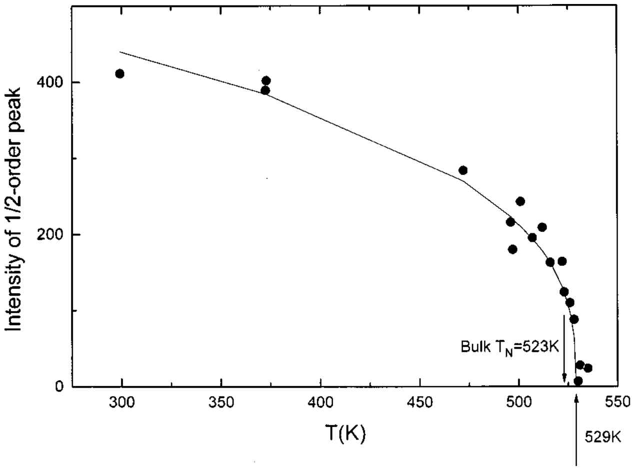

FIG. 9. Temperature dependence of the NiO(001) (1/2,0) magnetic peak intensity, showing a surface Néel temperature of 529 ±1 K; $T_N^b=523\,\mathrm{K}$ is indicated by an arrow. Solid circles are the experimental data, while the solid line $\propto I_1^2(B)$ fitted to the first and last experimental points.

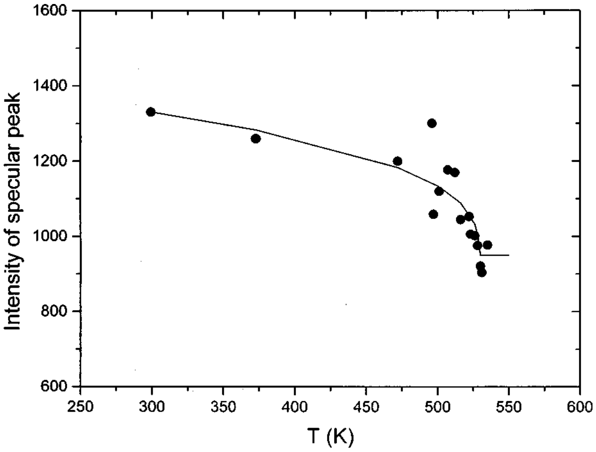

FIG. 10. Temperature dependence of the NiO(001) specular peak intensity, showing the same surface Néel temperature of 529 K. Solid circles are the experimental data, while the solid line $\propto I_0^2(B)$ fitted to the first and last experimental points.

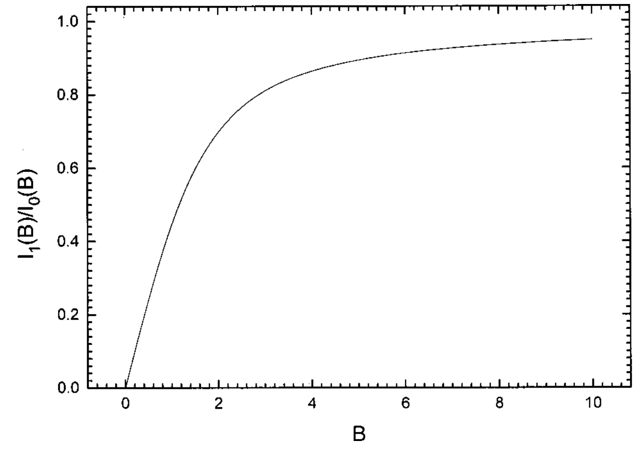

FIG. 11. $I_1(B)/I_0(B)$ vs the argument B.

data using a function of the form

$$\mathcal{I}_{(1/2,0)}=\mathcal{I}_{\mathrm{inc}}\mathcal{A}^*_{(\pi/a,0)}\mathcal{A}_{(\pi/a,0)}=\mathcal{I}_{\mathrm{inc}}\exp\left[-2W-\frac{2\alpha}{\tilde{q}_z}\right][I_1(B)]^2,$$

where $\mathcal{I}_{\mathrm{inc}}$ is the intensity of the incident beam. The data clearly indicate a surface critical Néel temperature $T_N^s=529\pm1$ K, different from the bulk Néel temperature $T_N^b=523.6$. Figure 10 shows the temperature dependence of the specular peak intensity, $\mathcal{I}_{(0,0)}$, which exhibits the same $T_N^s=529$ K, yet, by contrast, it approaches a nonzero magnitude above T_N^s. This agrees with the prediction of Eq. (10), and the fact that a nonmagnetic contribution to the specular peak is expected to be present. The solid curve is $\propto[I_0(B)]^2$, fitted to the first and last experimental points.

Since B includes the dependence of the sublattice magnetization on the reduced temperature (T/T_N), namely

$$B=\frac{\alpha s_0}{3\tilde{q}_z}\left(1-\frac{T}{T_N}\right)^{\beta_1}, \qquad (17)$$

we can obtain $B(T/T_N)$ from the ratio

$$\mathcal{R}(T)=\left(\frac{\mathcal{I}_{(1/2,0)}(T)}{\mathcal{I}_{(0,0)}(T)}\right)^{1/2}=\frac{I_1(B(T/T_N))}{I_0(B(T/T_N))} \qquad (18)$$

together with Fig. 11, which displays the ratio of the modified Bessel functions $I_1(B)/I_0(B)$ as a function of B. Note that in taking the ratio of the measured intensities, $\mathcal{I}_{(1/2,0)}/\mathcal{I}_{(0,0)}$, the factors e^{-W} and $e^{-\alpha/\tilde{q}_z}$ are eliminated. To determine the uncertainty in B, we first obtain the uncertainty $\sigma_{\mathcal{R}}$ in the ratio $\mathcal{R}(T)$ in terms of the uncertainties in the intensities of the specular and half-order peaks, namely

$$\sigma_{\mathcal{R}}=\frac{\mathcal{R}}{2}\left(\frac{1}{I_{(0,0)}}+\frac{1}{I_{(1/2,0)}}\right)^{1/2} \qquad (19)$$

and then make use of Fig. 11 to extract the uncertainties in the B values.

In Fig. 12(a) we show a plot of

$$\ln B=\ln\left(\frac{\alpha s_0}{3\tilde{q}_z}\right)+\beta_1\left[1-\left(\frac{T}{T_N}\right)\right] \qquad (20)$$

against the natural log of the reduced temperature, $1-(T/T_N^b)$, $T_N^b=523.6$ K. The apparent critical exponent for

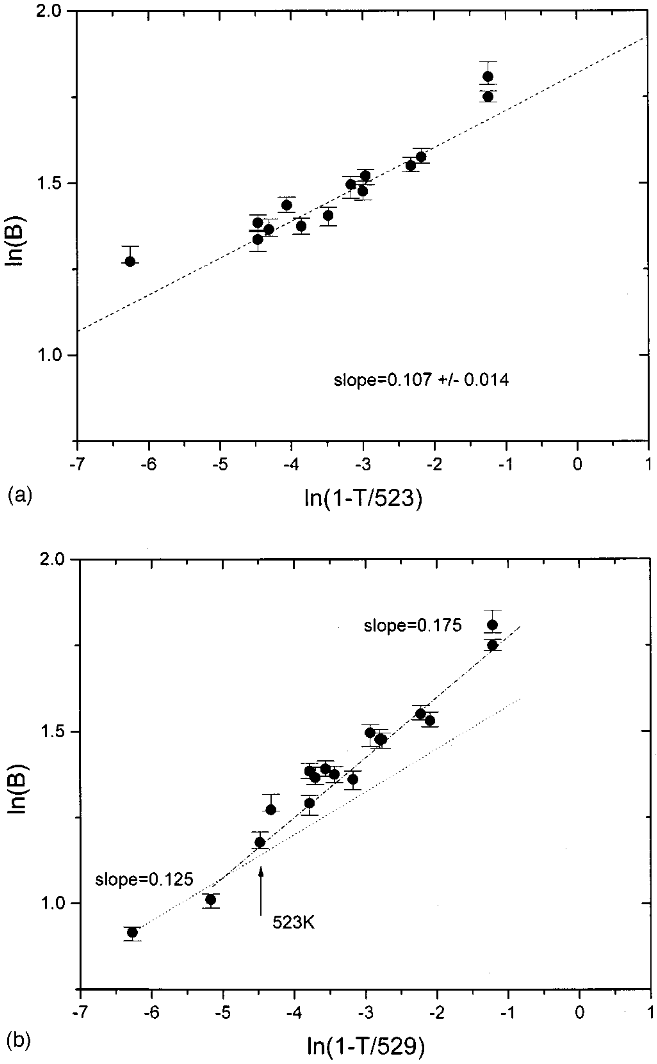

FIG. 12. (a) He* diffraction data fit to bulk critical temperature. (b) He* diffraction data fit to observed surface critical temperature.

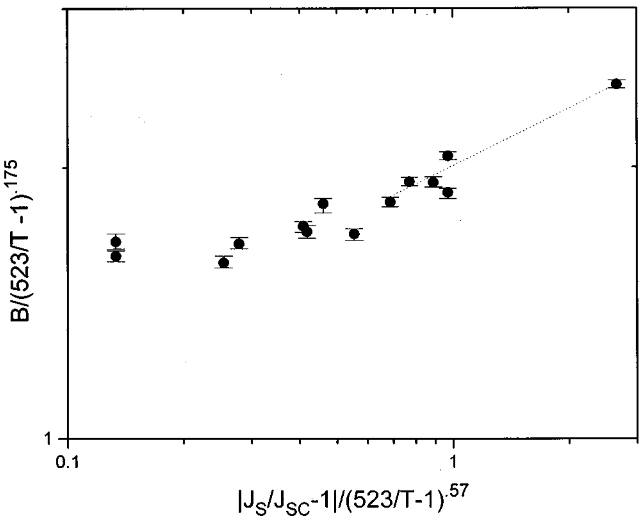

FIG. 13. Crossover scaling function obtained by plotting the reduced surface sublattice magnetization as a function of the crossover scaling variable $|J_s/J_{\mathrm{sc}}-1|(523/T-1)^{-0.57}$, $J_s^{\mathrm{eff}}/J_{\mathrm{sc}}=1.08$. The dashed line is the expected asymptotic behavior with a slope of 0.31.

the surface sublattice magnetization obtained from this plot (i.e., the slope of the best-fit line to the data) is 0.107 ± 0.014. Since this is smaller than the value that would correspond to a 2D Ising system, $\beta_1=0.125$, it becomes clear that this is an unphysical representation of the data. In Fig. 12(b), we plot $\ln B$ against $\ln[1-(T/T_N^s)]$, using the observed critical temperature, 529 K. The two dotted lines indicate the expected asymptotic behavior above and below $T_N^b=523.6\,\mathrm{K}$ for a system undergoing surface and extraordinary transitions. That is, below T_N^b the system should exhibit multicritical behavior asymptotically, characterized by the critical exponent 0.175. Above T_N^b, the system should asymptotically exhibit behavior corresponding to the surface transition, with a critical exponent of 0.125. While it is clear that more data are needed in the latter regime, the data below $T_N^b=523.6$ fit a slope of 0.175.

Figure 13 shows a plot of the reduced surface magnetization $B/(T_N^b/T-1)^{0.175}$ against the crossover scaling variable, $|J_s/J_{\mathrm{sc}}-1|/(523.6/T-1)^{\phi}$, with $\phi=0.57$, the crossover exponent derived by Diehl and Eisenriegler,[46] and a value of $|J_s/J_{\mathrm{sc}}-1|=0.08$ obtained from the scaling relation

$$\frac{J_s}{J_{\mathrm{sc}}}-1 \propto \left(\frac{T_N^s}{T_N^b}-1\right)^{\phi} \tag{21}$$

of Binder and Landau as shown in Figs. 2(a) and 16 of Refs. 27 and 28, respectively, using our experimental value of $T_N^s=529$. The dashed line is the linear asymptote with slope 0.31. The data clearly indicate a monotonically increasing crossover scaling function, quite similar to the upper branch of the surface crossover function obtained by Binder-Landau for the 3D Ising model, corresponding to the extraordinary transition. This is not surprising since the crossover scaling exponent derived by Binder and Landau for the 3D Ising model is $\phi=0.56$. We therefore conclude that the 3D Heisenberg model with surface anisotropy exhibits an anisotropic extraordinary transition with a critical behavior very similar to that of the 3D Ising model. Moreover, we ascertain that the manifestation of this behavior in our experimental data for the NiO(001) surface strongly supports and conforms with the enhanced surface Neél temperature that we obtain. We infer from these findings that the sublattice magnetization of NiO(001) undergoes a surface transition at 529 K and an extraordinary transition at the bulk Néel temperature 523.6 K. To our knowledge, this is the first observation of an extraordinary transition.

Recent results of Murthy and Sharma,[55] concerning the Neél temperatures of the (001) surface and bulk of the type-II rocksalt antiferromagnet, also support the scenario of $T_N^s > T_N^b$. Their calculations were based on a version of the SBMFT method[82–85] that proved quite successful in studies of frustrated quantum spin systems,[85] and was also applied recently to study the temperature dependence of the sublattice magnetization in the lamellar HT$_c$ copper oxides described by a quantum Heisenberg Hamiltonian with *XY* exchange and interlayer coupling.[86] The advantage of the SBMFT method is that *a priori* it assumes no particular order and, therefore, can describe both the ordered and disordered phases in a unified manner. Murthy and Sharma used a model with nearest-neighbor ferromagnetic J_1 and next-nearest-neighbor antiferromagnetic J_2 Heisenberg exchange. In order to account for the influence of the underlying substrate on the surface critical behavior, their most recent surface studies involved a four-layer system with surface single-site anisotropy D. A nice feature of this SBMFT calculation is that the mean-field ground state is disordered at any temperature if the site anisotropy is $D=0$, thus preserving an important aspect of the physics. This is in contrast to classical mean-field theories, which would predict a transition at a finite temperature in two dimensions even in the absence of a site anisotropy.

The results of the SBMF calculations for $D/J_2^s=0.1$ and $J_1^s/J_2^s=0.1$, which are the values consistent with both the known bulk values of J_1 and J_2 and our estimate of D, give $T_N^s=3.85J_2^s$ and $T_N^b=2.85J_2^b$, a trend in agreement with our measurements. There are two values of J_2^s on the surface currently proposed in the literature, $1.5J_2^b$ (Ref. 53) and $0.8J_2^b$.[54] The first of these gives $T_N^s=5.8J_2^b$, which is extremely high, while the second predicts $T_N^s=3.1J_2^b$, which is plausible experimentally. Thus, if we take the predictions of the SBMFT seriously, it suggests that the surface coupling is lower than that of the bulk. In order to obtain the experimentally observed ratio $T_N^s/T_N^b=1.012$, the surface coupling J_2^s should be $0.75J_2^b$, i.e., $J_2^s \simeq 15\,\mathrm{meV}$, compared to a bulk coupling of 19 meV.

When considering both the experimental results presented in this paper, and the theoretical results of Murthy and Sharma, we arrive at the following conclusions. The presence of single-site anisotropy, at the NiO(001) surface, leads to an Ising-like critical behavior, although in the strict sense this behavior belongs to the universality classes of the anisotropic special and extraordinary transitions. If we take this similarity at face value, we infer from the experimental results that the effective surface magnetic exchange coupling is about $J_2^s|_{\mathrm{eff}} \approx 1.08J_s^c = 1.6 \rightarrow 1.7J_2^b$, if we use the critical exchange coupling value of Binder and Landau. The moral inferred from our SBMFT calculations is that such enhancements in the effective Ising-type surface exchange coupling are readily achieved by the presence of the site anisotropy at the surface, even when the actual J_2^s is lower than J_2^b.

ACKNOWLEDGMENTS

The authors would like to acknowledge discussions with G. Murthy. This work was supported by the U.S. Department of Energy under Grant No. DE-FG02-85ER45222. The bulk specific-heat measurements were performed at the MRSEC Shared Facilities supported by the National Science Foundation under Grant No. DMR-9400334.

APPENDIX A: MAGNETIC PEAK AMPLITUDE IN THE EIKONAL APPROXIMATION

1. The eikonal approximation for a hard wall with dissipation

When the scattering wave function of the He* beam, Ψ, is expressed in terms of the action $\mathcal{S}$,

$$\Psi(\mathbf{r})=A\exp[i\mathcal{S}(\mathbf{r})/\hbar], \tag{A1}$$

the eikonal approximation corresponds to writing the action as[87]

$$\mathcal{S}_0(\mathbf{r})=p_z z-\frac{1}{v_z}\int_{z_0}^{z}V(\mathbf{R},z')dz' \tag{A2}$$

and the wave function Ψ becomes

$$\Psi(\mathbf{r})\sim A\exp\left\{i\left[\mathbf{k}\cdot\mathbf{r}-\frac{1}{\hbar v_z}\int_{z_0}^{z}V(\mathbf{R},z')dz'\right]\right\}. \tag{A3}$$

Considering the simple case of a hard corrugated wall, where the boundary conditions for the wave function require

$$\Psi(\mathbf{R},\zeta(\mathbf{R}))=0, \tag{A4}$$

where $\zeta(\mathbf{R})$ is the corrugation shape function, and adding the dissipative imaginary potential of Eq. (5), we arrive at

$$\psi(\mathbf{r})=A\exp\left\{i\big[\mathbf{K}\cdot\mathbf{R}+k_z\zeta(\mathbf{R})\big]-\frac{1}{\hbar v_z}\int_{z_0}^{z}V_I(\mathbf{R},z')dz'\right\}. \tag{A5}$$

2. The differential reflection coefficient and the correlation function

The differential reflection coefficient is written in terms of the transition operator $\hat{T}$ as[65–67]

$$\frac{d^2R}{\partial E\,\partial\Omega}=\frac{L^4M^2}{8\pi^3\hbar^5}\frac{v}{v_{iz}}\int_{-\infty}^{\infty}\exp\left(-i\frac{Et}{\hbar}\right)\times\langle\hat{T}^{\dagger}_{\mathbf{p}\leftarrow\mathbf{p_i}}(0)\hat{T}_{\mathbf{p}\leftarrow\mathbf{p_i}}(t)\rangle dt. \tag{A6}$$

The transition operator $\hat{T}$ is obtained using the scattering wave function expressed in the eikonal approximation. This approximation is justifiable in the present case because the velocity of the He* atoms is large compared to the velocity of the surface atoms, and in view of the small mass of the He* atom, its influence on the motion of the surface can be neglected. In this approximation, the transition matrix element becomes

$$\hat{T}_{\mathbf{p}\leftarrow\mathbf{p_i}}=-\frac{i\hbar^2k_{iz}}{ML^3}\int d\mathbf{R}\exp\left\{i[\mathbf{Q}\cdot\mathbf{R}+q_z\zeta(\mathbf{R})]-\frac{\alpha}{\tilde{q}_z}[1-(1/3)\xi(\mathbf{R})\langle\hat{S}_z(\mathbf{R})\rangle]\right\}, \tag{A7}$$

where $\alpha=MV_0z_0/\hbar^2$, $\mathbf{Q}=\mathbf{K}-\mathbf{K}_i$, $q_z=k_z-k_{iz}$, and $\tilde{q}_z=k_zk_{iz}/(k_z+k_{iz})$. Substituting into the differential reflection coefficient expression gives[66,67]

$$\frac{d^2R}{\partial E\,\partial\Omega}=\frac{k_{iz}k}{8\pi^3L^2\hbar}\int_{-\infty}^{\infty}dt\int d\mathbf{R}\,d\mathbf{R}'\times\exp\left\{-i\left[\frac{Et}{\hbar}+\mathbf{Q}\cdot(\mathbf{R}'-\mathbf{R})\right]\right\}\mathcal{C}(\mathbf{R},\mathbf{R}';t), \tag{A8}$$

where $\mathcal{C}(\mathbf{R},\mathbf{R}';t)$ is the correlation function

$$\mathcal{C}(\mathbf{R},\mathbf{R}';t)=\left\langle\exp\left[-iq_z\zeta(\mathbf{R}';0)-\frac{\alpha}{\tilde{q}_z}\{1-\tfrac{1}{3}\xi(\mathbf{R}')\langle\hat{S}_z(\mathbf{R}')\rangle\}\right]\times\exp\left[iq_z\zeta(\mathbf{R};t)-\frac{\alpha}{\tilde{q}_z}\{1-\tfrac{1}{3}\xi(\mathbf{R})\langle\hat{S}_z(\mathbf{R})\rangle\}\right]\right\rangle. \tag{A9}$$

In order to introduce the Debye-Waller factor, we follow the recipe of Levi *et al.*[66,67] and split the corrugation shape function $\zeta(\mathbf{R},t)$ into a static part $\zeta_0(\mathbf{R})$ and a time-dependent part $v(\mathbf{R},t)$:

$$\zeta(\mathbf{R},t)=\zeta_0(\mathbf{R})+v(\mathbf{R},t), \tag{A10}$$

where $v(\mathbf{R},t)$ is given by

$$v(\mathbf{R},t)=u_z(\mathbf{R},t)+\mathbf{U}(\mathbf{R},t)\cdot\boldsymbol{\nabla}\zeta_0(\mathbf{R}), \tag{A11}$$

where $\mathbf{u}=(\mathbf{U},u_z)$ is the thermal displacement. The correlation function then becomes

$$\mathcal{C}(\mathbf{R},\mathbf{R}';t)=\exp\left\{-iq_z[\zeta_0(\mathbf{R}')-\zeta_0(\mathbf{R})]+\frac{\alpha}{3\hat{q}_z}[\xi(\mathbf{R}')\langle\hat{S}_z(\mathbf{R}')\rangle+\xi(\mathbf{R})\langle\hat{S}_z(\mathbf{R})\rangle]\right\}\times\exp\left[-\frac{2\alpha}{\hat{q}_z}\right]\times\langle\exp[-iq_zv(\mathbf{R}',0)]\exp[iq_zv(\mathbf{R},t)]\rangle. \tag{A12}$$

The term $\langle\,\rangle$ is calculated in the traditional way by quantizing the normal modes of the surface motion $v(\mathbf{R},t)$ to obtain

$$\begin{aligned}\mathcal{C}(\mathbf{R},\mathbf{R}';t)=\exp\Bigg\{&-iq_z[\zeta_0(\mathbf{R}')-\zeta_0(\mathbf{R})]\\ &+\frac{\alpha}{3\tilde{q}_z}[\xi(\mathbf{R}')\langle\hat{S}_z(\mathbf{R}')\rangle+\xi(\mathbf{R})\langle\hat{S}_z(\mathbf{R})\rangle]\Bigg\}\\ &\times\exp\left[-\frac{2\alpha}{\tilde{q}_z}\right]\exp\{-\tfrac{1}{2}q_z^2[\langle v^2(\mathbf{R})\rangle\\ &+\langle v^2(\mathbf{R}')\rangle]\}\exp[-q_z\langle v(\mathbf{R}',0)v(\mathbf{R},t)\rangle]\\ =\mathcal{A}^*(\mathbf{R}')&\mathcal{A}(\mathbf{R})\exp[-q_z\langle v(\mathbf{R}',0)v(\mathbf{R},t)\rangle],\end{aligned} \tag{A13}$$

where the terms $\exp\{-\frac{1}{2}q_z^2[\langle v^2(\mathbf{R})\rangle+\langle v^2(\mathbf{R}')\rangle]\}$ is just the Debye-Waller term $\exp[-2W]$. The elastic contribution is then obtained by setting $E=0$ in the differential reflection coefficient expression, or, alternatively, by taking $t\rightarrow\infty$ in the correlation function

$$\mathcal{C}(\mathbf{R},\mathbf{R}';\infty)=\mathcal{A}^*(\mathbf{R}')\mathcal{A}(\mathbf{R}), \tag{A14}$$

with

$$\mathcal{A}(\mathbf{R})=\exp\left\{iq_z\zeta_0(\mathbf{R})-W-\frac{\alpha}{\tilde{q}_z}[1-(1/3)\xi(\mathbf{R})\langle\hat{S}_z(\mathbf{R})\rangle]\right\}. \tag{A15}$$

Substituting back in the differential reflection coefficient expression, we get

$$\left(\frac{d^2R}{\partial E\,\partial\Omega}\right)_{\text{elastic}}\simeq\frac{k_{iz}k}{4\pi^2L^2}\,\delta(E)\left|\int d\mathbf{R}\exp(\mathbf{Q}\cdot\mathbf{R})\mathcal{A}(\mathbf{R})\right|^2. \tag{A16}$$

Making use of the surface periodicity, the modulus squared can be written as

$$4\pi^2\frac{L^2}{\Omega}d^2(\mathbf{Q}-\mathbf{G})\left|\int_{\text{u.c.}}d\mathbf{R}\exp(\mathbf{Q}\cdot\mathbf{R})\mathcal{A}(\mathbf{R})\right|^2, \tag{A17}$$

where u.c. stands for unit cell and Ω is its area. We thus obtain the differential reflection coefficient

$$\left(\frac{d^2R}{\partial E\,\partial\Omega}\right)_{\text{elastic}}\simeq k_{iz}k\sum_{\mathbf{G}}\delta^2(\mathbf{Q}-\mathbf{G})\,\delta(E)|\tilde{\mathcal{A}}_{\mathbf{G}}|^2, \tag{A18}$$

where

$$\begin{aligned}\tilde{\mathcal{A}}_{\mathbf{G}}=\frac{1}{\Omega}\int_{\text{u.c.}}d\mathbf{R}\exp\Bigg\{&i[\mathbf{G}\cdot\mathbf{R}+q_z\zeta(\mathbf{R})]\\ &-W-\frac{\alpha}{\tilde{q}_z}[1-(1/3)\xi(\mathbf{R})\langle\hat{S}_z(\mathbf{R})\rangle]\Bigg\}.\end{aligned} \tag{A19}$$

---

[1] C. G. Shull, W. A. Strauser, and E. O. Wollan, Phys. Rev. **83**, 333 (1951).

[2] T. Nagamiya, K. Yosida, and R. Kubo, Adv. Phys. **4**, 1 (1955).

[3] W. L. Roth, Phys. Rev. **110**, 1333 (1958); **111**, 772 (1958).

[4] W. L. Roth, J. Appl. Phys. **31**, 2000 (1960).

[5] E. Uchida, N. Fukuoka, H. Kondoh, T. Takeda, Y. Nakazumi, and T. Nagamiya, J. Phys. Soc. Jpn. **23**, 1197 (1967).

[6] T. Yamada, J. Phys. Soc. Jpn. **31**, 664 (1966).

[7] T. Yamada, S. Saito, and Y. Shimomura, J. Phys. Soc. Jpn. **21**, 672 (1966).

[8] A. P. Cracknell, *Magnetism in Crystalline Materials* (Pergamon, Oxford, 1975), and references therein.

[9] S. J. Joshua, *Symmetry Principles and Magnetic Symmetry in Solid State Physics* (IOP, Bristol, 1991), and references therein.

[10] P. W. Anderson, Phys. Rev. **79**, 350 (1950).

[11] P. W. Anderson, Science **235**, 1196 (1987).

[12] M. T. Hutchings and E. J. Samuelson, Phys. Rev. B **6**, 3447 (1972).

[13] H. P. Rooksby, Acta Crystallogr. **1**, 26 (1948).

[14] I. Negovetić and J. Konstantinović, Solid State Commun. **13**, 249 (1973).

[15] M. E. Lines, Phys. Rev. **135**, A1336 (1964).

[16] M. E. Lines, Phys. Rev. **139**, A1304 (1965).

[17] D. L. Mills, Phys. Rev. B **3**, 3887 (1971).

[18] T. Wolfram, R. E. de Wames, W. F. Hall, and P. W. Palmberg, Surf. Sci. **28**, 45 (1971).

[19] T. C. Lubensky and M. H. Rubin, Phys. Rev. B **12**, 3885 (1975).

[20] K. Binder and P. C. Hohenberg, Phys. Rev. B **6**, 3461 (1972).

[21] K. Binder and P. C. Hohenberg, Phys. Rev. B **9**, 2194 (1974).

[22] K. Binder and D. P. Landau, Surf. Sci. **61**, 577 (1976).

[23] A. J. Bray and M. A. Moore, J. Phys. A **10**, 1927 (1977).

[24] K. Binder, in *Phase Transitions and Critical Phenomena*, edited by C. J. Domb and J. L. Lebowitz (Academic, London, 1986), Vol. 8, and references therein.

[25] H. W. Diehl, in *Phase Transitions and Critical Phenomena*, edited by C. J. Domb and J. L. Lebowitz (Academic, London, 1988), Vol. 10, and references therein.

[26] A. J. Bray and M. A. Moore, Phys. Rev. Lett. **38**, 1046 (1977).

[27] K. Binder and D. P. Landau, Phys. Rev. Lett. **52**, 318 (1984); Phys. Rev. B **41**, 4633 (1990); **41**, 4786 (1990).

[28] M. Pleimling and W. Selke, Eur. Phys. J. B **1**, 385 (1998).

[29] H. W. Diehl and M. Shpot, Phys. Rev. Lett. **73**, 3431 (1994); Nucl. Phys. B **528**, 595 (1998).

[30] T. C. Lubensky and M. H. Rubin, Phys. Rev. Lett. **31**, 1469 (1973).

[31] T. C. Lubensky and M. H. Rubin, Phys. Rev. B **11**, 4533 (1975).

[32] H. W. Diehl and S. Dietrich, Phys. Lett. **80A**, 375 (1980).

[33] H. W. Diehl and S. Dietrich, Z. Phys. B **42**, 65 (1981); **43**, 281(E) (1981).

[34] H. W. Diehl and S. Dietrich, Phys. Rev. B **24**, 2878 (1981).

[35] H. W. Diehl and S. Dietrich, Z. Phys. B **50**, 117 (1983).

[36] P. W. Palmberg, R. E. de Wames, and L. A. Vredevoe, Phys. Rev. Lett. **21**, 682 (1968).

[37] P. W. Palmberg, R. E. de Wames, L. A. Vredevoe, and T. Wolfram, J. Appl. Phys. **40**, 1158 (1969).

[38] T. Wolfram, R. E. de Wames, W. F. Hall, and P. W. Palmberg, Surf. Sci. **28**, 45 (1971).

[39] K. Namikawa, T. Wolfram, K. Hayakawa, and S. Miyake, J. Phys. Soc. Jpn. **37**, 733 (1974).

[40] K. Namikawa, J. Phys. Soc. Jpn. **44**, 165 (1978).

[41] Anna Swan, W. Franzen, M. El-Batanouny, and K. M. Martini, in *The Structure of Surfaces III*, edited by C. Y. Tong, M. A. van

Hove, and K. Takayanagi (Springer, Berlin, 1991), p. 190.

[42] Anna Swan, W. Franzen, M. El-Batanouny, and K. M. Martini, in *Advances in Surface and Thin Film Diffraction*, edited by T. C. Huang, P. I. Cohen, and D. J. Eaglesham, Materials Research Society Symposia Proceedings. No. 208 (MRS, Pittsburgh, 1991), p. 273.

[43] A. Swan, M. Marynowski, W. Franzen, M. El-Batanouny, and K. M. Martini, Phys. Rev. Lett. **71**, 1250 (1993).

[44] A. Swan, M. Marynowski, W. Franzen, M. El-Batanouny, and K. M. Martini, J. Vac. Sci. Technol. A **12**, 2219 (1994).

[45] M. Marynowski, A. Swan, W. Franzen, M. El-Batanouny, and K. M. Martini, Surf. Interface Anal. **23**, 105 (1995).

[46] H. W. Diehl and E. Eisenriegler, Phys. Rev. B **30**, 300 (1984).

[47] S. Alvarado, M. Campagna, and H. Hopster, Phys. Rev. Lett. **48**, 51 (1982).

[48] S. Alvarado, M. Campagna, F. Ciccacci, and H. Hopster, J. Appl. Phys. **53**, 7920 (1982).

[49] C. Rau and S. Eichner, in *Nuclear Methods in Materials Research*, edited by K. Bedge, H. Bauman, H. Jex, and F. Rauch (Vieweg, Braunschweig, 1980), p. 354; C. Rau, J. Magn. Magn. Mater. **31-34**, 874 (1983).

[50] D. Weller, S. Alvarado, W. Gudat, K. Schröder, and M. Campagna, Phys. Rev. Lett. **54**, 1555 (1985).

[51] H. Tang, D. Weller, T. G. Walker, J. C. Scott, C. Chappert, H. Hopster, A. W. Pang, D. S. Dessau, and D. P. Pappas, Phys. Rev. Lett. **71**, 444 (1993).

[52] C. Rau, C. Jin, and M. Robert, Phys. Lett. A **138**, 334 (1989).

[53] J. J. M. Pothuizen, O. Cohen, and G. A. Sawatzky, in *Epitaxial Oxide Thin Films II*, edited by J. S. Speck, D. K. Fork, R. M. Wolf, and T. Shiosaki, Materials Research Society Symposia Proceedings No. 401 (MRS, Pittsburgh, 1996), p. 501.

[54] C. de Graaf, R. Broer, and W. C. Nieuwport, Chem. Phys. Lett. **271**, 372 (1997).

[55] G. Murthy and P. Sharma, private communications and unpublished.

[56] J. W. Locke, UTIAS Report No. 143 (1969).

[57] R. S. Van Dyke, Jr., C. E. Johnson, and H. A. Shugart, Phys. Rev. A **4**, 1327 (1971).

[58] W. Sesselmann, B. Woratschek, J. Kuppers, G. Ertl, and H. Haberland, Phys. Rev. B **35**, 1547 (1987).

[59] H. Conrad, G. Ertl, J. Kuppers, W. Sesselmann, B. Woratschek, and H. Haberland, Surf. Sci. **121**, 161 (1982).

[60] H. Conrad, G. Ertl, J. Kuppers, W. Sesselmann, B. Woratschek, and H. Haberland, Surf. Sci. **117**, 98 (1982).

[61] *Deexcitation and Neutratization Processes*, H. D. Hagstrum, in *Inelastic Ion-Surface Collisions*, edited by N. H. Tolk, J. C. Tully, and C. W. White (Academic, New York, 1977), p. 1.

[62] W. Sesselmann, H. Conrad, G. Ertl, J. Kuppers, B. Woratschek, and H. Haberland, Phys. Rev. Lett. **50**, 446 (1983).

[63] L. A. Salmi, Phys. Rev. B **46**, 4180 (1992).

[64] M. Marynowski, W. Franzen, and M. El-Batanouny, Rev. Sci. Instrum. **65**, 3718 (1994).

[65] U. Garibaldi, A. C. Levi, R. Spadacini, and G. E. Tommei, Surf. Sci. **38**, 269 (1973).

[66] A. C. Levi and H. Suhl, Surf. Sci. **88**, 221 (1979).

[67] A. C. Levi, Nuovo Cimento B **54**, 357 (1979).

[68] P. Cantini, R. Tatarek, and G. P. Felcher, Phys. Rev. B **19**, 1161 (1979).

[69] J. P. Toennies, G. Witte, A. M. Shikin, and K. H. Rieder, J. Electron Spectrosc. Relat. Phenom. **64/65**, 677 (1993).

[70] W. P. Brug, G. Chern, J. Duan, G. G. Bishop, S. A. Safron, and J. G. Skofronick, unpublished and private communications.

[71] G. Witte, P. Senet, and J. P. Toennies, unpublished and private communications.

[72] A. Drewitz, R. Leidl, T. W. Burkhardt, and H. W. Diehl, Phys. Rev. Lett. **78**, 1090 (1997).

[73] P. Czerner and U. Ritschel, Int. J. Mod. Phys. B **11**, 2075 (1997).

[74] P. C. Hohenberg, Phys. Rev. **158**, 383 (1967).

[75] N. D. Mermin and H. Wagner, Phys. Rev. Lett. **17**, 1133 (1966).

[76] M. El-Batanouny, G. Murthy, C. R. Willis, S. Kais, and V. Staemmler, Phys. Rev. B **58**, 7391 (1998).

[77] C. Wang, K. Fink, and V. Staemmler, Chem. Phys. **192**, 25 (1995).

[78] G. A. Sawatzky and J. W. Allen, Phys. Rev. Lett. **53**, 2339 (1984).

[79] J. M. McKay and V. E. Henrich, Phys. Rev. Lett. **53**, 2343 (1984).

[80] B. Koiller and L. M. Falicov, J. Phys. C **7**, 299 (1974).

[81] B. Bleaney and K. W. H. Stevens, Rep. Prog. Phys. **16**, 108 (1953).

[82] See, for example, A. Auerbach, *Interacting Electrons and Quantum Magnetism* (Springer-Verlag, New York, 1994).

[83] D. Arovas and A. Auerbach, Phys. Rev. Lett. **61**, 617 (1988); Phys. Rev. B **38**, 316 (1988).

[84] I. Affleck and J. B. Marston, Phys. Rev. B **37**, 3774 (1988); J. B. Marston and I. Affleck, *ibid.* **39**, 11 538 (1989); J. B. Marston and C. Zeng, J. Appl. Phys. **69**, 5962 (1991).

[85] N. Read and S. Sachdev, Phys. Rev. Lett. **66**, 1773 (1991); S. Sachdev and N. Read, Int. J. Mod. Phys. B **5**, 219 (1991); S. Sachdev, Phys. Rev. B **45**, 12 377 (1992).

[86] B. Keimer, A. Aharony, A. Auerbach, R. J. Birgeneau, A. Cassanho, Y. Endoh, R. W. Erwin, M. A. Kastner, and G. Shirane, Phys. Rev. B **45**, 7430 (1992).

[87] L. I. Schiff, *Quantum Mechanics*, 3rd ed. (McGraw-Hill, New York, 1968), p. 339.